mathematics

Article

Morphology of Hybrid MHD Nanofluid Flow through Orthogonal Coaxial Porous Disks

Qadeer Raza [1,†], M. Zubair Akbar Qureshi [1], Bagh Ali [2], Ahmed Kadhim Hussein [3,4], Behzad Ali Khan [1], Nehad Ali Shah [5,†] and Wajaree Weera [6,*]

1 Department of Mathematics, Multan Campus, AIR University, Multan 49501, Pakistan
2 Faculty of Computer Science and Information Technology, Superior University, Lahore 54000, Pakistan
3 Mechanical Engineering Department, College of Engineering, University of Babylon, Hilla 00964, Iraq
4 College of Engineering, University of Warith Al-Anbiyaa, Karbala 56001, Iraq
5 Department of Mechanical Engineering, Sejong University, Seoul 05006, Korea
6 Department of Mathematics, Faculty of Science, Khon Kaen University, Khon Kaen 40002, Thailand
* Correspondence: wajawe@kku.ac.th
† These authors contributed equally to this work and are co-first authors.

Abstract: In this article, we study the novel features of morphological effects for hybrid nanofluid flow subject to expanding/contracting geometry. The nanoparticles are incorporated due to their extraordinary thermal conductivity and innovative work for hybrid nanofluids, which are assembled of aluminum oxides, Al_2O_3 metallic oxides, and metallic copper Cu. Cu nanoparticles demonstrate very strong catalytic activity, while Al_2O_3 nanoparticles perform well as an electrical insulator. The governing partial differential equations of the elaborated model are transformed into a system of nonlinear ordinary differential equations with the use of similarity variables, and these equations are numerically solved through a shooting technique based on the Runge–Kutta method. We develop a hybrid correlation for thermophysical properties based on a single-phase approach. A favorable comparison between shape and size factors for metallic and metallic-oxide nanoparticles is discussed via tables and figures. Moreover, the effect of embedding flow factors on concentration, velocity, and temperature is shaped in line with parametric studies, such as the permeable Reynolds number, nanoparticle volume fractions, and expansion/contraction parameters. The fluid velocity, temperature, and concentration are demonstrated in the presence of hybrid nanoparticles and are discussed in detail, while physical parameters such as the shear stress, flow of heat, and mass transfer at the lower and upper disks are demonstrated in a table. The hybrid nanoparticles show significant results as compared to the nanofluids. If we increase the nanoparticle volume fraction, this increases the thermal performance for an injection/suction case as well. The above collaborative research provides a strong foundation in the field of biomedical equipment and for the development of nanotechnology-oriented computers.

Keywords: morphology effect; hybrid nanoparticles; orthogonal porous disks

MSC: 76D05; 76W05; 76-10

Citation: Raza, Q.; Qureshi, M.Z.A.; Ali, B.; Hussein, A.K.; Khan, B.A.; Shah, N.A.; Weera, W. Morphology of Hybrid MHD Nanofluid Flow through Orthogonal Coaxial Porous Disks. *Mathematics* **2022**, *10*, 3280. https://doi.org/10.3390/math10183280

Academic Editors: Juan Francisco Sánchez-Pérez, Gonzalo García Ros and Manuel Conesa

Received: 17 August 2022
Accepted: 5 September 2022
Published: 9 September 2022

1. Introduction

The morphology of nanomaterials has proved effective in influencing the actions of nanomaterials under optical waves and photons. Similarly, the particle form influences nanoparticle (NP) movement in the circulatory system, immunological responses, and activity within internalized cells. Furthermore, the asymmetry of NPs induces particle chipping and rounding along the underflow walls of blood vessels. It also causes NP penetration and distribution in tumors and tissues. Furthermore, due to a diversity of reactions with the cell surface, NPs of diverse sizes and shapes might accumulate differently inside the same cell. Non-spherical NPs also prefer to stay in the blood as compared to spherical ones, as indicated by their higher blood circulation duration. The absorption efficiency of rod-shaped NPs is also superior to that of cubical, cylindrical, and spherical ones. Spherical NPs can be processed quickly after internalization, have acute margination effects, and have quicker blood circulation than other shapes. However, rod-shaped NPs show a comparatively slower processing time after internalization and can enter solid-tissue tumors with comparative ease, as discussed by Qureshi et al. [1]. Zeeshan et al. [2] investigated the various forms of NPs floating across a spinning disk on combined convection past steady flow. For a nanofluid (*Nfd*), the base fluid is known to be copper NPs of disk, cylindrical, and spherical types of varying sizes and water. Haq et al. [3] studied the completely formed *Nfd* pressing flux between parallel disks. They found three separate forms of condensed NPs in the base fluid. These NPs were Magnetite (Fe_3O_4), Mn–Zn ferrite (Mn–Zn Fe_2O_4), and cobalt ferrite ($CoFe_3O_4$). The movement and heat transfer of copper NPs embedded in the base fluid were studied by Khan et al. [4]. They included water as a liquid basis. They found a template for the thermal conductivity of *Nfd*s by Hamilton and Crosser. The research is known to be done in three types of NPs, namely, platelet-, cylinder-, and brick-shaped particles. By including a mathematical decrease at the mainline level, Ashraf et al. [5] investigated computer modeling of continuous natural convection flow in the presence of a strong magnetic field and a weak magnetic quantity of Prandtl. The findings regarding the mathematical diffusion coefficient, related magnetic field, and buoyant body energy were used in the momentum equation to generate a series of boundary layer equations before moving on to the computer simulation.

It is evident from the literature that unified transfer of heat and mass, from diverse geometries, has massive engineering and geophysical implications, including in geothermal reservoirs, drying of porous solids, enhanced oil recovery, thermal insulation, and underground species transport. Heat and mass transfer are relevant in the many varieties of thermodynamic devices, such as pumps, compressors, turbines, nozzles, diffusers, refrigeration systems, air conditioning systems, microwave ovens, conventional ovens, and coffee makers, as discussed by Qureshi et al. [6]. This drew the attention of researchers towards such a combined process. Devi et al. [7] analyzed the motion of an electrically conductive fluid that is affected by thermal radiation and is surrounded by an infinite rotating porous disk with heat and mass transfer. On the contrary, unsteady mixed convection of a hybrid nanofluid (*HNfd*) due to a rotating disk was also observed. Accordingly, Hang Xu et al. [8] presented a generalized homogenous flow model, explaining *HNfd* as incorporating diversified versions of NPs, as a construct to model these issues. Moreover, Mabood et al. [9] investigated the effect of the fraction volume on metallic or metallic-oxide NPs + H_2O, radiation, viscous dissipation, and chemical reaction, including magnetohydrodynamic (MHD) heat and mass transfer stagnation point flow. The flow over a revolving disk on *HNfd* reveals the character of the Hall current, which was represented in another study by Acharya et al. [10]. Acharya et al. [11] studied the properties of heat and fluid movement in the form of thermophoretic transport; a numerical simulation was developed based on nonlinear paired partial differential equations respecting the conservation rules. A thermophoretic transport term is incorporated in the mass equation; hence, the influence of thermophoretic transport may be measured at various sphere locations. Hussain et al. [12] developed this by keeping a porous disk on metallic NPs, which addressed many issues due to the convection of heat and mass transfer of an incompressible viscous *Nfd* in a mathematical model. Das et al. [13] mathematically investigated a couple of connecting disks with a magnetic field and slip effect squeezed by the flow of *Nfd*. The equivalent disk on squeezed MHD flow of a *Nfd* is affected by both velocity and temperature slip, as discussed by Mohyud-Din et al. [14]. On a floating plane surface, Erickson et al. [15] observed the permeable expansion ratio and the collective effect of heat and mass transfer. On the other hand, the regular thermal conduction boundary layer flow and the heat and mass exchange of *Nfd*, which are influenced by several factors such as the size, shape, and kind of *Nfd*, as well as the type and operating temperature of the base fluid, were observed by Zakari et al. [16]. Turkyilmazoglu et al. [17] developed fluid flow and heat transfer as the by-product of a disk, rotating both upward and downward, during uneven motion. It was also found that this upward and downward movement of the disk exerts a similar effect to permeability across the wall, albeit with identifiable differences.

Correspondingly, the role of magnetic orientation is monumental in affecting heat transport in *HNfd*. Likewise, emerging technologies including biotechnology, electrical engineering, and electromechanics have a more positive role in the case of magnetic field influence. Transformers, generators, and electric motors are useful applications of magnetic fields. For thermally conductive fluid, certain investigators researched the issue of magnetohydrodynamic (MHD) boundary layer flow, heat, and mass transfer among different layer geometries. Temperature profile contraction was observed with increased merits of heat energy deposition under layer constraint when Mutuku et al. [18] noticed an unsteady MHD boundary layer, temperature, and concentration profile of *Nf* over a surface with dual deposition in the layers. Sudarsana Reddy et al. [19,20] analyzed the MHD physical thermal conduction boundary layer flow, heat, and mass transfer features of a pair of separated *Nfd*s, across a rotation disk and vertical cone, along with the chemical reaction. The free heat thermal conduction and mass transfer were measured in nanoliquid MHD flow through an irregular thickness across a slender elastic surface by Ashraf et al. [21]. Lou et al. [22] considered the micropolar dusty fluid with the dynamic effect of MHD rotating fluid. Several researchers have discussed heat and mass transfer and MHD boundary layer flow attributes across multiple geometries [23,24].

Choi [25] coined the idea of *Nfd*s (the mixing of nanosized solid particles in base fluids) with higher thermal conductivity in comparison to the routine fluids available. Furthermore, the size of a *Nfd* plays a pivotal role in bringing stability to it, with a size of less than 100 nm considered a stable size for *Nfd*. Resultantly, *Nfd* has a handful of practical utilities as well, including in industrial cooling, paper, biomedicine, chemical reactors, and many more. Recent research has started considering *HNfd*s (containing two or more NPs) in place of ordinary *Nfd*s because of their similar yet comparatively superior performance outcomes. Nimmagadda and Priyadharshini et al. [26,27] measured an emerging concept in technology-related work. The viscosity and heat energy conductivity of an Al_2O_3-Cu/H_2O *HNfd* was calculated. Suresh et al. [28] showed that with a solid volume fraction of Al_2O_3-Cu NPs, all parameters were increased. In the same way, Sarkar et al. [29] brought the attention of researchers to the area of *HNfd*s. Moghadassi et al. [30] studied the effects of Al_2O_3-H_2O *Nfd*, along with the effects of Al_2O_3-Cu/H_2O *HNfd*, showing that Al_2O_3-Cu/H_2O *HNfd* had greater heat transfer. This was followed by the analytical and numerical investigation of *HNfd* conducted by Huminic and Huminic et al. [31]. Ashraf et al. [32] investigated the effect of radiation on the continuous, viscous, and electrically conductive mixed-convection boundary layer movement of fluid over a semi-infinite porous longitudinally magnetized magnet with uniform sweat and a variable cross-cut magnetic field on the top.

In porous media, the presence of extensive fluid interaction surfaces can enhance the heat transmission effect. The porous medium alters the flow field conditions, thins the frontal layer, and typically has a higher conduction heat transfer coefficient than the fluid under study. Numerous technical applications, including polymeric, ceramic, and metallic foams, have made heat transmission in porous media a hot research area. For the past few decades, flow in porous medium has been the focus of active research. The effects of capillary forces and the kind of wettability of the medium on the displacement process were addressed in [33,34], which evaluated the process of imbibition in a porous medium under the influence of capillary forces in microgravity. The authors of [35–37] proposed a non-stationary mathematical model of multiphase fluid flow and computationally modeled the removal of a viscous fluid from a porous material while accounting for capillary effects in a sample of a porous medium. The temperature and velocity profiles above condensed material were theoretically determined within the framework of boundary layer approximation under the assumption of fuel gasification and gas-phase chemicals reacting in a diffusion flame. Logvinov et al. [38] investigated the removal of a viscous fluid from a rectangular Hele-Shaw cell. Tyurenkova et al. [39] studied the rate of material surface regression in turbulent and laminar flow regimes.

A review of the literature revealed to the authors that no research has been done on heat and mass transfer analysis of MHD incompressible hybrid nanofluid flow subject to two porous coaxial discs that are moving orthogonally. Thermal conductivity is most commonly described by form factors, and the viscosity model is developed as a hybrid model of thermophysical properties that depend on the size factors. These facts served as the impetus for the research herein, which was done to account for two distinct categories of nanomaterials and to depict a fully formed hybrid nanofluid that moves across porous disks in a strong magnetic field. The system was simplified to multiple related nonlinear ordinary differential equations (ODEs) that regulate the flow of an electromagnetic hydrodynamic hybrid nanofluid between orthogonal porous disks. Numerical calculation was performed to solve the system of ordinary differential equations via Runge–Kutta shooting techniques with the help of MATLAB software.

2. Mathematical Formulation

In this paper, the single-phase approach was used to model the *HNfd* because the single-phase model is more suitable for Newtonian fluid and its thermophysical properties based on the NP volume of the fraction. It is also called the experimental model [40]. The detailed *HNfd* thermophysical properties used in this paper are shown in Table 1, and Table 2 presents the thermophysical properties of the basic fluid and NPs. Due to their significant amount of essential porous structure, the Cu NPs exhibit very robust catalytic efficiency. Al_2O_3 NPs are an insulating material, but ceramic material has rather good heat transparency. In a comparison of both NP types, the thermal conductivity of Cu NPs is relatively higher than that of Al_2O_3.

Table 1. Thermophysical properties of HN_{fd} [41].

Properties	Hybrid Nanofluid (Cu–Al_2O_3–Water)
Density (ρ)	$\rho_{hnf} = \varphi_1\rho_{s_1} + \varphi_2\rho_{s_2} - (1-\varphi_1-\varphi_2)\,\rho_{bf}$
Viscosity (μ)	$\mu_{hnf} = \mu_{bf}\left(1+0.1008\left((\varphi_1)^{0.69574}(dp_1)^{0.44708} + (\varphi_2)^{0.69574}(dp_2)^{0.44708}\right)\right)$
Heat Capacity (ρC_P)	$(\rho c_p)_{hnf} = \varphi_1(\rho c_p)_{s_1} + \varphi_2(\rho c_p)_{s_2} + (1-\varphi_1-\varphi_2)\,(\rho c_p)_{bf}$
Thermal Conductivity (K)	$k_{hnf} = \frac{k_{s2}+(N-1)k_{mbf}-(N-1)\varphi_2(k_{mbf}-k_{s2})}{k_{s2}+(N-1)k_{mbf}+\varphi_2(k_{mbf}-k_{s2})}k_{mbf}$ Where $k_{mbf} = \frac{k_{s1}+(N-1)k_{bf}-(N-1)\varphi_1(k_{bf}-k_{s1})}{k_{s1}+(N-1)k_{bf}+\varphi_1(k_{bf}-k_{s1})}k_{bf}$

Table 2. Thermophysical properties of base fluid and NPs [42].

Title	H_2O (f)	$Al_2O_3(\varphi_1)$	Cu(φ_2)
ρ ($\mathrm{kgm^{-3}}$)	997.0	3970	8933
C_p ($\mathrm{J\,kg^{-1}k^{-1}}$)	4180	765	385
κ ($\mathrm{wm^{-1}k^{-1}}$)	0.6071	40	400

A two-dimensional Newtonian hybrid MHD nanofluid flow (Al_2O_3–Cu/water) was considered between the deformable porous disks with cylindrical coordinates (r, θ, z); this was chosen as it can be proved as a most appropriate prototype for morphology analysis of heat and mass transfer. The fluid is incompressible, unsteady, isothermal, and laminar. The porous walls expand and contract up- and downward. The geometry was developed with significant modification as shown in Figure 1. The channel walls can move up and down at time-dependent rate $k'(t)$ with range $2k(t)$. The resulting magnetic field B_0 is disregarded under the minimal Reynolds number supposition. Terms T_1, T_2, C_1, and C_2 denote the temperature and concentration at the lower and upper permeable disks, correspondingly, with $T_1 > T_2$ and $C_1 > C_2$. The laws of conservation of mass, momentum, energy, and concentration are expressed as follows [43]:

$$\frac{\partial u}{\partial r}+\frac{u}{r}+\frac{\partial w}{\partial z}=0, \tag{1}$$

$$\frac{\partial u}{\partial t}+u\frac{\partial u}{\partial r}+w\frac{\partial u}{\partial z}=-\frac{1}{\rho_{hnf}}\frac{\partial p}{\partial r}+v_{hnf}\left(\frac{\partial^2 u}{\partial r^2}+\frac{1}{r}\frac{\partial u}{\partial r}-\frac{u}{r^2}+\frac{\partial^2 u}{\partial z^2}\right)-\frac{\sigma_e B_0^2}{\rho_{hnf}}u, \tag{2}$$

$$\frac{\partial w}{\partial t}+u\frac{\partial w}{\partial r}+w\frac{\partial w}{\partial z}=-\frac{1}{\rho_{hnf}}\frac{\partial p}{\partial z}+v_{hnf}\left(\frac{\partial^2 w}{\partial r^2}+\frac{1}{r}\frac{\partial w}{\partial r}+\frac{\partial^2 w}{\partial z^2}\right), \tag{3}$$

$$\frac{\partial T}{\partial t}+u\frac{\partial T}{\partial r}+w\frac{\partial T}{\partial z}=\alpha_{hnf}\frac{\partial^2 T}{\partial z^2}, \tag{4}$$

$$\frac{\partial C}{\partial t}+u\frac{\partial C}{\partial r}+w\frac{\partial C}{\partial z}=D_{hnf}\frac{\partial^2 C}{\partial z^2}, \tag{5}$$

where B_0^2 is the intensity of the magnetic field, p denotes pressure, σ_e denotes electrical conductivity, T denotes the temperature, v_{hnf} is the kinematic viscosity of HN_{fd}, ρ_{hnf} is the density of HN_{fd}, α_{hnf} is the thermal diffusivity of HN_{fd}, and D_{hnf} represents the diffusion coefficient of HN_{fd}. The initial boundary conditions for the lower and upper boundaries are:

$$\left.\begin{array}{lllll} z_1=-k(t), & u=0, & w=-A_1k'(t), & T=T_1, & C=C_1, \\ z_1=k(t), & u=0, & w=A_1k'(t), & T=T_2 & C=C_2. \end{array}\right\} \tag{6}$$

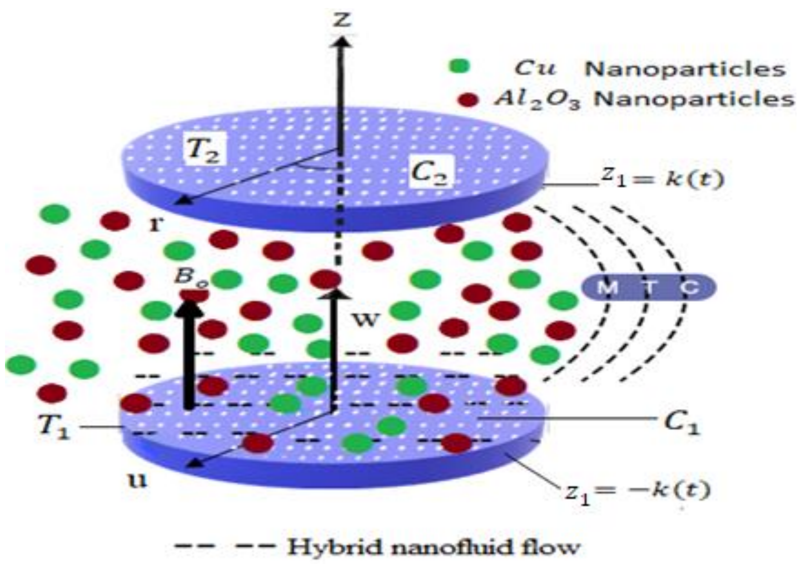

Figure 1. Physical model.

Here, A_1 is the measure of partition penetrability, and the prime symbol denotes the derivative with respect to time t.

To continue the investigation, we provide the following set of transformation variables [43].

$$\left.\eta=\frac{z_1}{k}, u=-\frac{rv_f}{k^2}F_\eta(\eta,t), w=\frac{2v_f}{k}F(\eta,t), \quad \theta=\frac{T-T_2}{T_1-T_2}, \quad \chi(\eta)=\frac{C-C_2}{C_1-C_2}.\right\} \tag{7}$$

The continuity Equations (1) and (5) were fulfilled using the similarity transformation. Consequently, Equations (1)–(5) were transformed into the dimensionless forms:

$$\frac{v_{hnf}}{v_f}F_{\eta\eta\eta\eta}+\alpha\left(3F_{\eta\eta}+\eta F_{\eta\eta\eta}\right)-2FF_{\eta\eta\eta}-\frac{k^2}{v_f}F_{\eta\eta t}-\frac{\rho_f}{\rho_{hnf}}\mathrm{M}F_{\eta\eta}=0, \tag{8}$$

$$\theta_{\eta\eta}+\frac{v_f}{\alpha_{hnf}}(\alpha\eta-2F)\theta_\eta-\frac{k^2}{\alpha_{hnf}}\theta_t=0, \tag{9}$$

$$\chi_{\eta\eta}+Sc\,(\alpha\eta-2F)\chi'-k^2\chi_t=0. \tag{10}$$

where $\alpha=\frac{kk'(t)}{v_f}$ is the wall expansion ratio, $\mathrm{Re}=\frac{A_1kk'(t)}{2v_f}$ is the permeable Reynolds number, $Sc=\frac{v_f}{D}$ is the Schmidt number, $v_{hnf}=\frac{\mu_{hnf}}{\rho_{hnf}}$ is the kinematic viscosity of hybrid nanofluid, $\alpha_{hnf}=\frac{k_{hnf}}{(\rho c_p)_{hnf}}$ is the thermal diffusivity of hybrid nanofluid, $Pr=\frac{(\mu C_p)_{bf}}{k_{bf}}$ is the Prandtl number, and $\mathrm{M}=\frac{\sigma_e B_0^2k^2}{\mu_f}$ is the magnetic parameter.

The dimensionless physical limitations listed below were considered:

$$\left.\begin{array}{r}\eta=-1,\ F=-Re, F_\eta=0,\theta=1,\ \chi=1,\\ \text{and}\ \ \eta=1,\ F=Re, F_\eta=0,\theta=0,\ \chi=0.\end{array}\right\} \tag{11}$$

Finally, Majdalani et al. [44] set F = f Re, α is a constant, $f=f(\eta)$, $\theta=\theta(\eta)$, and $\chi=\chi(\eta)$, which leads to $\theta_t=0$, $f_{\eta\eta t}=0$, and $\chi_t=0$. Thus, we have the following equations:

$$\frac{v_{hnf}}{v_f}f_{\eta\eta\eta\eta}+\alpha\left(3f_{\eta\eta}+\eta f_{\eta\eta\eta}\right)-2Ref f_{\eta\eta\eta}-\frac{\rho_f}{\rho_{hnf}}\mathrm{M}f_{\eta\eta}=0, \tag{12}$$

$$\theta_{\eta\eta}+\left((1-(\varphi_1+\varphi_2))+(\varphi_1)\left(\frac{\rho_{cps_1}}{\rho_{cpbf}}\right)+(\varphi_2)\left(\frac{\rho_{cps_2}}{\rho_{cpbf}}\right)\right)\frac{k_{mbf}}{k_{hnf}}\frac{k_{bf}}{k_{mbf}}Pr(\alpha\eta-2Ref)\theta_\eta=0, \tag{13}$$

$$\chi''+Sc(\alpha\eta-2fRe)\chi'=0. \tag{14}$$

$$\left.\begin{array}{r}\eta=-1,\ \ f=-1,\ f_\eta=0,\theta=1,\ \chi=1,\\ \eta=1,\ f=1,\ f_\eta\ =0,\theta=0\ \chi=0.\end{array}\right\} \tag{15}$$

Quantities of engineering interest: Skin friction, the Nusselt number, and the Sherwood number are physical parameters that are crucial to the technical goal of modeling equipment at the nanoscale. All of these variables were estimated on both porous surfaces.

Skin friction coefficients: Skin friction coefficients for the lower and upper discs are represented by the variables C_{f1} and C_{f-1} and are stated as

$$C_{f-1}=\frac{\zeta_y|_{\eta=-1}}{\rho_f(s'A)^2}=\frac{\left(1+0.1008\left((\varphi_1)^{0.69574}(dp_1)^{0.44708}+(\varphi_2)^{0.69574}(dp_2)^{0.44708}\right)\right)}{Re_r}f''(-1), \tag{16}$$

$$C_{f1}=\frac{\zeta_y|_{\eta=1}}{\rho_f(s'A)^2}=\frac{\left(1+0.1008\left((\varphi_1)^{0.69574}(dp_1)^{0.44708}+(\varphi_2)^{0.69574}(dp_2)^{0.44708}\right)\right)}{Re_r}f''(1),$$

where ξ_{zr} represents the shear stress at the lower and upper discs in the radial direction, and $Re_r=4\left(\frac{k}{r}\right)\left(\frac{1}{Re}\right)^2$ stands for the local Reynolds number.

$$\zeta_y=\mu_{hnf}\left(\frac{\partial u}{\partial y}\right)|_{\eta=-1}=\mu_{bf}\left(1+0.1008\left((\varphi_1)^{0.69574}(dp_1)^{0.44708}+(\varphi_2)^{0.69574}(dp_2)^{0.44708}\right)\right)\left(\frac{rv_f}{s^3}\right)f''(-1),$$

$$\zeta_y=\mu_{hnf}\left(\frac{\partial u}{\partial y}\right)|_{\eta=1}=\mu_{bf}\left(1+0.1008\left((\varphi_1)^{0.69574}(dp_1)^{0.44708}+(\varphi_2)^{0.69574}(dp_2)^{0.44708}\right)\right)\left(\frac{rv_f}{s^3}\right)f''(1).$$

Nusselt numbers: The ratio of conductive to convective heat flow inside a fluid at a boundary is known as the Nusselt number (Nu). Fluid movement (advection) and diffusion are components of convection (conduction). A Nusselt number of 1 represents pure conduction as the mode of heat transfer. The analysis of the heat transfer rates (Nusselt numbers) $Nu_{\eta=-1}$ and $Nu_{\eta=1}$ at the lower and upper discs is provided as

$$Nu|_{\eta=-1} = \frac{ks_z}{\kappa_f(T_1 - T_2)}|_{\eta=-1} = -\frac{k_{hnf}}{k_f}\theta'(-1),$$

$$Nu|_{\eta=1} = \frac{ks_z}{\kappa_f(T_1 - T_2)}|_{\eta=1} = -\frac{k_{hnf}}{k_f}\theta'(1), \tag{17}$$

where heat flux is denoted by s_z, which follows as

$$s_z|_{\eta=-1} = -k_{hnf}\left(\frac{\partial T}{\partial z}\right)|_{\eta=-1} = -\frac{(T_1 - T_2)}{k}k_{hnf}\theta'(-1),$$

$$s_z|_{\eta=1} = -k_{hnf}\left(\frac{\partial T}{\partial z}\right)|_{\eta=1} = -\frac{(T_1 - T_2)}{k}k_{hnf}\theta'(1).$$

Sherwood numbers: The proportion of convectional mass transfer to diffusional mass transfer is known as the Sherwood number. The following mathematical equations describe the mass transfer rates (Sherwood numbers) $Sh|_{\eta=-1}$ and $Sh|_{\eta=1}$ at the lower and upper discs:

$$Sh|_{\eta=-1} = \frac{kq_z}{D_{hnf}(C_1 - C_2)}|_{\eta=-1} = -\chi'(-1),$$

$$Sh|_{\eta=1} = \frac{kq_z}{D_{hnf}(C_1 - C_2)}|_{\eta=1} = -\chi'(1), \tag{18}$$

where

$$q_z|_{\eta=-1} = -D_{hnf}\left(\frac{\partial C}{\partial z}\right)|_{\eta=-1} = -D_{hnf}\frac{(C_1 - C_2)}{k}\chi'(-1),$$

$$q_z|_{\eta=1} = -D_{hnf}\left(\frac{\partial C}{\partial z}\right)|_{\eta=1} = -D_{hnf}\frac{(C_1 - C_2)}{k}\chi'(1),$$

where $Re = \frac{A_1kk'(t)}{2v_f}$.

Numerical Solution Procedure: To obtain numerical solutions for the transformed ODEs (12)–(14) with suitable transformed boundary conditions (15), Runge–Kutta and the efficient "shooting method" approach were taken into consideration. With this approach, the necessary dimensionless ODEs were simply handled. The nonlinear particle differential problem was transformed into a highly nonlinear linked system of ordinary differential equations, forming Equations (12)–(14).

$$\begin{gathered}\left(\frac{\left(1+0.1008\left((\varphi_1)^{0.69574}(dp_1)^{0.44708}+(\varphi_2)^{0.69574}(dp_2)^{0.44708}\right)\right)}{\left((1-(\varphi_1+\varphi_2))+(\varphi_1)\left(\frac{\rho s_1}{\rho_{bf}}\right)+(\varphi_2)\left(\frac{\rho s_2}{\rho_{bf}}\right)\right)}\right)f''''[\eta]+\alpha(3f''[\eta]+\eta f'''[\eta])-2Ref[\eta]f'''[\eta]- \\ \left(\frac{1}{\left((1-\varphi_1-\varphi_2)+\varphi_1\left(\frac{\rho s_1}{\rho_{bf}}\right)+\varphi_2\left(\frac{\rho s_2}{\rho_{bf}}\right)\right)}\right)\mathrm{M}\,f''[\eta]=0,\end{gathered} \tag{19}$$

$$\begin{aligned}&\theta''[\eta] \\ &+\left((1-(\varphi_1+\varphi_2))+(\varphi_1)\left(\frac{\rho_{cps_1}}{\rho_{cpbf}}\right)\right. \\ &\left.+(\varphi_2)\left(\frac{\rho_{cps_2}}{\rho_{cpbf}}\right)\right)\left(\frac{k_{s2}+(N-1)k_{mbf}+\varphi_2\left(k_{mbf}-k_{s2}\right)}{k_{s2}+(N-1)k_{mbf}-(N-1)\varphi_2\left(k_{mbf}-k_{s2}\right)}\right)\left(\frac{k_{s1}+(N-1)k_{bf}+\varphi_1\left(k_{bf}-k_{s1}\right)}{k_{s1}+(N-1)k_{bf}-(N-1)\varphi_1\left(k_{bf}-k_{s1}\right)}\right) \\ &\qquad Pr(\alpha\eta-2Ref[\eta])\theta'[\eta]=0,\end{aligned} \tag{20}$$

$$\chi''[\eta] + \mathrm{Sc}(\alpha\eta - 2\mathrm{Re}f[\eta])\chi'[\eta] = 0, \tag{21}$$

Here, we assume that

$$H_1 = \left(\frac{\left(1 + 0.1008\left((\varphi_1)^{0.69574}(dp_1)^{0.44708} + (\varphi_2)^{0.69574}(dp_2)^{0.44708}\right)\right)}{\left((1 - (\varphi_1 + \varphi_2)) + (\varphi_1)\left(\frac{\rho_{s_1}}{\rho_{bf}}\right) + (\varphi_2)\left(\frac{\rho_{s_2}}{\rho_{bf}}\right)\right)} \right),$$

$$H_2 = \left(\frac{1}{\left((1 - \varphi_1 - \varphi_2) + \varphi_1\left(\frac{\rho_{s_1}}{\rho_{bf}}\right) + \varphi_2\left(\frac{\rho_{s_2}}{\rho_{bf}}\right)\right)} \right),$$

$$H_3 = \left((1 - (\varphi_1 + \varphi_2)) + (\varphi_1)\left(\frac{\rho_{cps_1}}{\rho_{cpbf}}\right) + (\varphi_2)\left(\frac{\rho_{cps_2}}{\rho_{cpbf}}\right) \right),$$

$$D_1 = \left(\frac{k_{s2} + (N-1)k_{mbf} + \varphi_2\left(k_{mbf} - k_{s2}\right)}{k_{s2} + (N-1)k_{mbf} - (N-1)\varphi_2\left(k_{mbf} - k_{s2}\right)} \right),$$

$$D_2 = \left(\frac{k_{s1} + (N-1)k_{bf} + \varphi_1\left(k_{bf} - k_{s1}\right)}{k_{s1} + (N-1)k_{bf} - (N-1)\varphi_1\left(k_{bf} - k_{s1}\right)} \right),$$

$\omega = D_1 D_2$.

Putting values of H_1, H_2, H_3, D_1, D_2, and ω in Equations (19)–(21), we obtain the final result as follows:

$$H_1 f''''[\eta] + \alpha(3f''[\eta] + \eta f'''[\eta]) - 2Ref[\eta]f''[\eta] - H_2\mathrm{M}\, f''[\eta] = 0, \tag{22}$$

$$\theta''[\eta] + H_3\omega Pr(\alpha\eta - 2Ref[\eta])\theta'[\eta] = 0, \tag{23}$$

$$\chi''[\eta] + \mathrm{Sc}(\alpha\eta - 2\mathrm{Re}f[\eta])\chi'[\eta] = 0. \tag{24}$$

To solve the existing flow model, we used the RK technique with the addition of shooting methods. The following substitution is required to begin the process:

$$w_1 = f[\eta],\ w_2 = f'[\eta],\ w_3 = f''[\eta],\ w_4 = f'''[\eta], w_5 = \theta[\eta],\ w_6 = \theta'[\eta],\ w_7 = \chi[\eta],\ w_8 = \chi'[\eta]. \tag{25}$$

First, in Equations (22)–(24), we change the model in the following pattern:

$$f''''[\eta] = \frac{1}{H_1}(-\alpha(3f''[\eta] + \eta f'''[\eta]) + 2Ref[\eta]f''[\eta] + H_2\mathrm{M}\, f''[\eta]), \tag{26}$$

$$\theta''[\eta] = -\left(H_3\omega Pr\left(\alpha\eta - 2Ref[\eta]\theta'[\eta]\right)\right), \tag{27}$$

$$\chi''[\eta] = \mathrm{Sc}(-\alpha\eta + 2\mathrm{Re}f[\eta])\chi'[\eta],$$

The following system is obtained by using the substitution contained in Equation (25):

$$\begin{bmatrix} w_1' \\ w_2' \\ w_3' \\ w_4' \\ w_5' \\ w_6' \\ w_7' \\ w_8' \end{bmatrix} = \begin{bmatrix} w_2 \\ w_3 \\ w_4 \\ \frac{1}{H_1}(-\alpha(3w_3 + \eta w_4) + 2Rew_1 w_3 + H_2\mathrm{M}\, w_3) \\ w_6 \\ -(H_3\omega Pr(\alpha\eta - 2Rew_1)w_6) \\ w_7 \\ \mathrm{Sc}(2Rew_1 - \alpha\eta)w_8 \end{bmatrix}, \tag{28}$$

Consequently, the initial condition is:

$$\begin{bmatrix} w_1' \\ w_2' \\ w_3' \\ w_4' \\ w_5' \\ w_6' \\ w_7' \\ w_8' \end{bmatrix} = \begin{bmatrix} -1 \\ 0 \\ 1 \\ 0 \\ 1 \\ 0 \\ 1 \\ 0 \end{bmatrix}. \tag{29}$$

The above system was then solved using mathematics and a suitable initial condition. Here, Runge–Kutta and the well-known accurate "shooting method" were taken into consideration. The required dimensionless ODEs can easily be tackled with this method. First of all, we obtained the initial condition by using the shooting method in such a way that boundary conditions were satisfied and achieved the desired level of accuracy.

3. Results and Discussion

To understand the problem, we must carry out a numerical evaluation of the non-linear differential equations. The impact of relevant physical parameters like the expansion/contraction ratio parameter (α), permeable Reynolds parameter (Re), Prandtl number (Pr), shape factor (N), magnetic parameter (M), Schmidt number (Sc), diameter of NPs $(dp_1$ and $dp_2)$, and volume friction parameter $(\varphi_1$ and $\varphi_2)$ on the velocity, temperature, and concentration profiles is shown graphically in Figures 2–9. We validated our findings against previously published research articles using Table 3 before visualizing the results. An excellent coincidence was obtained, confirming the validity of the method. The current analysis was produced by entering the following values for the parameters: $Re = 1,\ \varphi_2 = 0.01,\ dp_1 = 0.01,\ dp_2 = 0.021,$ and $M = 1$. The competitive contrast gives support to the recorded numerical performance.

Table 3. Comparison of results regarding the heat transfer rate at the lower disk for $Re = 0,\ \varphi_2 = 0, M = 0$.

		Kashif et al. [45]	Present Results	Kashif et al. [45]	Present Results
φ	φ_1	$\alpha < 0$	$\alpha < 0$	$\alpha > 0$	$\alpha > 0$
0%	0%	3.16640	3.16650	1.67941	1.67956
5%	5%	3.61121	3.61130	1.91744	1.91749
10%	10%	4.16060	4.16071	2.21351	2.21378
15%	15%	4.84304	4.84315	2.58392	2.58399
20%	20%	5.69882	5.69893	3.05193	3.051989

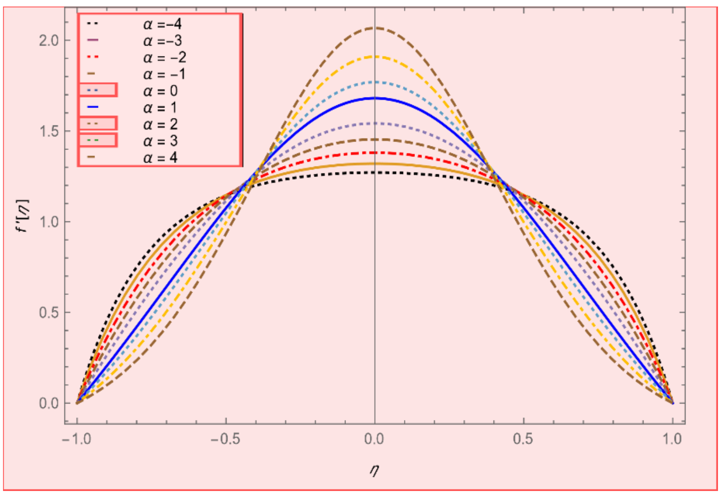

Figure 2. Radial velocity profiles for $\varphi_1 = \varphi_2 = 0.01,\ Sc = 1, M = 1, Re = -1,\ Pr = 6.2$.

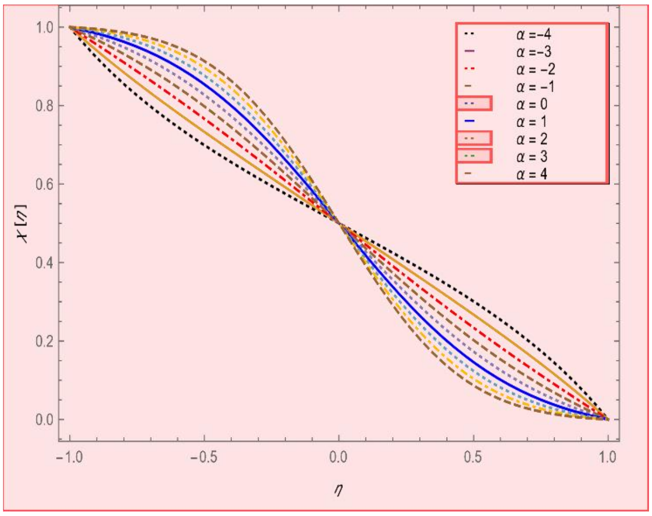

Figure 3. Concentration profiles for $\varphi_1 = \varphi_2 = 0.01,\ Sc = 1, M = 1, Re = -1,\ Pr = 6.2$.

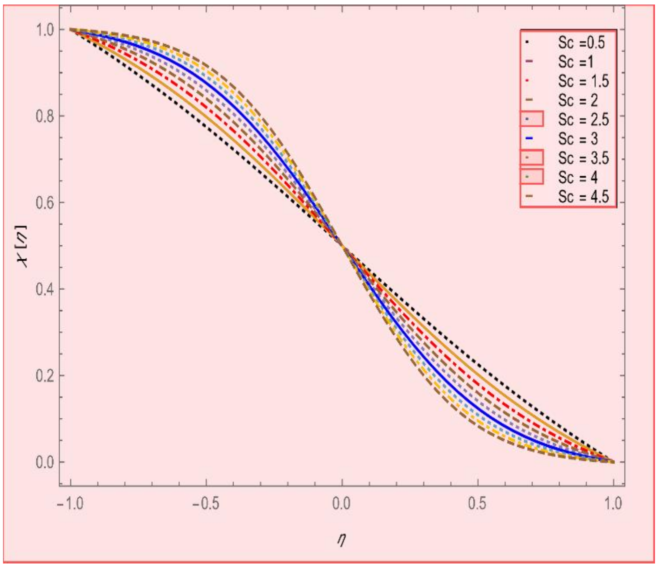

Figure 4. Concentration profiles for $\varphi_1 = \varphi_2 = 0.01,\ \alpha = 1, M = 1, Re = 1,\ Pr = 6.2$.

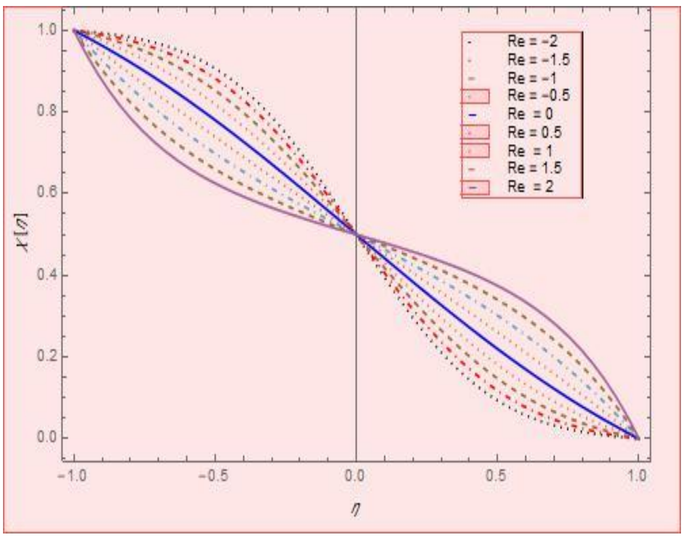

Figure 5. Concentration profiles for $\varphi_1 = \varphi_2 = 0.01,\ \alpha = -1, M = 1, Sc = 1,\ Pr = 6.2$.

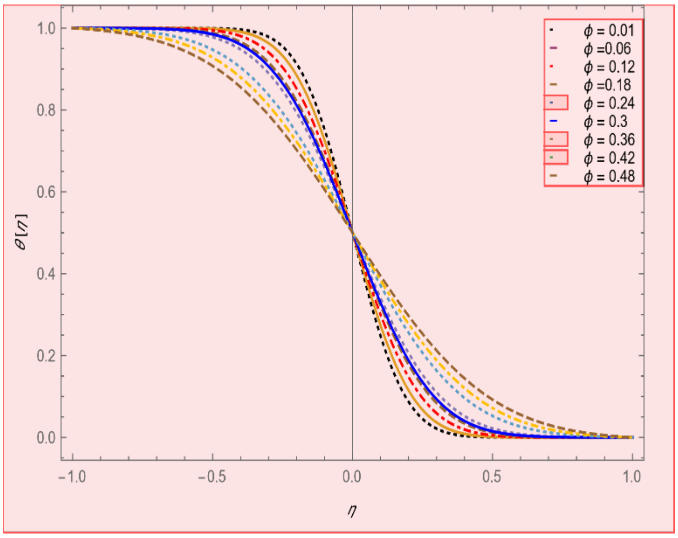

Figure 6. Temperature profiles for volume fraction $\alpha = 4, M = 1, Re = -1,\ Pr = 6.2$.

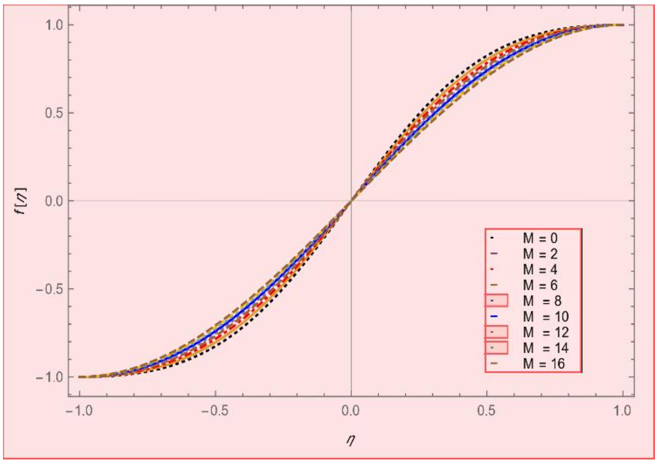

Figure 7. Axial velocity profile for $\varphi_1 = \varphi_2 = 0.01, \alpha = 1,\ Re = -1$.

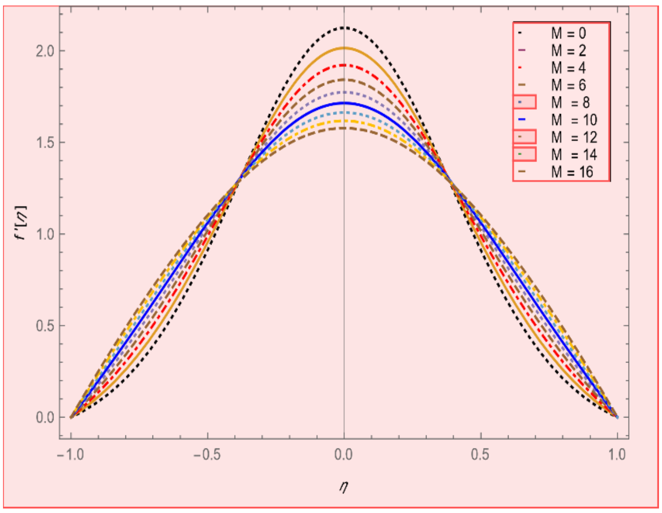

Figure 8. Radial velocity profile for $\varphi_1 = \varphi_2 = 0.01, \alpha = 1,\ Re = -1$.

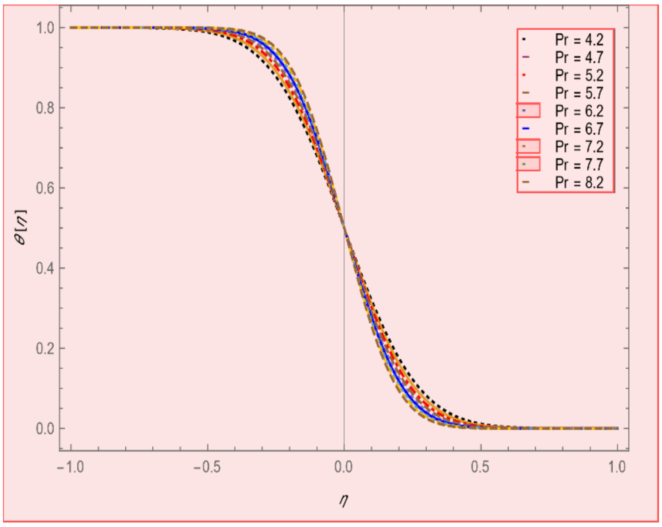

Figure 9. Temperature profile for the effect of the Prandtl number, $\varphi_1 = \varphi_2 = 0.04, \alpha = 3,\ Re = -1,$ $M = 1, Sc = 1$.

3.1. Effect of Variable Shear Stress ($f'(\eta)$), Heat Transfer ($\theta'(\eta)$), Mass Transfer ($\chi(\eta)$), and Thermal Conductivity of Hybrid Nanofluid (k_{hnf})

Table 4 presents the impact of different parameters like α, Re, φ_1, φ_2, M, dp_1, and dp_2 on the shear stress for both porous disks with hybrid nanofluid (Al_2O_3 + Cu/H_2O). Increasing the values of α, φ_1, φ_2 dp_1, and dp_2 decreased the shear stress, but an opposite effect was observed for $Re,\ M$ for the upper and lower disks. Table 5 indicates the effect of parameters $Pr,\ N$, and α on heat transfer flow at the upper and lower disks. By enhancing the values of N and α, the heat transfer flow rate was reduced, but Pr had the opposite impact for both porous disks. The mass transfer flow effect with Sc, Re, and α for both porous disks with HN_{fd} is shown in Table 6. Table 6 shows that with increasing Sc and Re values, the flow behavior of the mass transfer rate also increased for both porous disks, but the reverse was observed for α for the upper and lower disks. Table 7 shows the effect of the volume fractions φ_1 and φ_2 for similar shapes (spherical, plates, bricks, cylindrical) and size factors of NPs. If we raise the values of volume fractions φ_1 and φ_2, the thermal conductivity of the hybrid nanofluid (Al_2O_3 + Cu/H_2O) is increased in several types of shape factor but is much better in terms of thermal conductivity rate for the platelet shape factor.

Table 4. Calculations of the effect of shear stress at the lower and upper disks for Al_2O_3 + Cu/H_2O HN_{fd} for different nondimensional parameters.

Al_2O_3 + Cu/H_2O								
α	φ_1	φ_2	Re	M	dp_1	dp_2	$\|f'(-1)\|$	$\|f'(1)\|$
1				1	0.01	0.01	2.86822	2.86822
2			1				1.82187	1.82187
3	0.01 = 1%	0.01 = 1%					0.77265	0.77265
4							0.29907	0.29907
	0.02 = 2%	0.01 = 1%	1	1			2.86178	2.86178
1	0.03 = 3%						2.85581	2.85581
	0.04 = 4%						2.85028	2.85028
1	0.01 = 1%	0.02 = 2%	1	1			2.84421	2.84421
		0.03 = 3%					2.82103	2.82103
		0.04 = 4%					2.79874	2.79874

Table 4. *Cont.*

				$Al_2O_3 + Cu/H_2O$				
α	φ_1	φ_2	Re	M	dp_1	dp_2	$\lvert f'(-1)\rvert$	$\lvert f'(1)\rvert$
1	0.01 = 1%	0.01 = 1%	2				3.72387	3.72387
			3				5.00722	5.00722
			4				6.67346	6.67346
				2			3.09975	3.09975
1	0.01 = 1%	0.01 = 1%	1	3			3.31576	3.31576
				4			3.51844	3.51844
					0.05		5.241	5.241
					0.1		5.237	5.237
					0.15		5.233	5.233
					0.05	0.05	5.241	5.241
1	0.01 = 1%	0.01 = 1%	1	1		0.1	5.237	5.237
						0.15	5.233	5.233

Table 5. Heat transfer rates at the lower and upper disks for Al_2O_3 + Cu/H_2O HN_{fd}.

			$Al_2O_3 + Cu/H_2O$	
Pr	N	α	$\lvert\theta'(-1)\rvert$	$\lvert\theta'(1)\rvert$
5	3	1	2.20736	2.20736
5.7			2.52049	2.52049
6.2			2.74784	2.74784
7			3.11511	3.11511
6.2	3	1	3.00884	3.00884
	3.7		2.9688	2.9688
	4.9		2.90299	2.90299
	5.7		2.86822	2.86822
6.2	3	1	3.00884	3.00884
		2	1.03645	1.03645
		3	0.20387	0.20387
		4	0.02797	0.02797

Table 6. Simulation results of the numerical impact of flow mass transfer at the lower and upper disks for Al_2O_3 + Cu/H_2O HN_{fd}.

			$Al_2O_3 + Cu/H_2O$	
Sc	Re	α	$\lvert\chi(-1)\rvert$	$\lvert\chi(1)\rvert$
1			0.77628	0.77628
2	1	1	1.13597	1.13597
3			1.56842	1.56842
4			2.05396	2.05396
1	1		0.77628	0.77628
	2	1	1.43009	1.43009
	3		2.26351	2.26351
	4		3.1994	3.1994
	1	1	0.77628	0.77628
1		2	0.58169	0.58169
		3	0.43021	0.43021
		4	0.31574	0.31574

Table 7. Numerical results on the thermal conductivity k_{hnf} of HN_{fd} given different shape and size factors.

$(Al_2O_3–Cu/H_2O)$					
***N*=Shape and Size Factor**		***N*=3**	***N*=3.7**	***N*=4.8**	***N*=5.7**
φ_1	φ_2	k_{hnf}	k_{hnf}	k_{hnf}	k_{hnf}
0.01 = 1%	0.01 = 1%	0.236201	0.23873	0.24260	0.24566
0.02 = 2%		0.020056	0.021461	0.02372	0.025623
0.03 = 3%		0.000103	0.000129	0.00017	0.0002306
0.04 = 4%		0.000009	0.0000128	0.000021	0.000031
0.01 = 1%	0.02 = 2%	0.020096	0.021544	0.02412	0.025898
	0.03 = 3%	0.000101	0.000128	0.000187	0.000237
	0.04 = 4%	0.000008	0.000013	0.000022	0.000032

3.2. Velocity and Temperature Profile Effects of α, M, Re, Pr, and φ

Figure 2 shows the effect of the expansion/contraction parameter α varying from negative to positive; the radial velocity fluid flow rose from the center of the wall but was reduced by the momentum boundary layer thickness for both porous disks. Furthermore, in all expanding/contracting cases, the fluid flow decelerated and, in effect, induced a decrease in velocity near the profile. The line graph flows symmetrically. Figure 6 shows that increasing the values of both volume fractions ($\varphi = \varphi_1$ and φ_2) enhanced the thermal boundary layer thickness flow for the upper disk but with the opposite flow of fluid in the lower disk. The NPs physically disperse heat. Applying many NPs at the same time expends more energy, increasing the levels and thickness of the temperature field. Figures 7 and 8 present the increasing behavior of the middle of the wall of the axial and radial velocity profiles through the impact of magnetic parameter M when it is greater than 0. We may conclude from these results that the transversal absorption magnetic field normalizes the fluid velocity. The magnetic effect causes the vibration of the particles inside the fluid, which is governed by the Lorentz force. Therefore, increasing the value of M decreases the pattern of the internal wall but increases the momentum boundary layer thickness in the radial velocity profile. Figure 9 demonstrates the *Pr* number's impact on the temperature profile. The ratio of thermal diffusivity to momentum diffusivity is defined as the Prandtl number. With increasing values of *Pr*, the flow of fluid thermal boundary layer thickness was reduced from the upper disk, and the opposite flow of fluid occurred in the lower disk, as shown in Figure 9.

3.3. Concentration Profile Effects of α,Sc and Re

Figure 3 shows that the impact of α values varied from negative to positive on the concentration profile. At large values of α, the impact on the flow of mass transfer was opposite in the upper and lower disks. The evolution of the concentration field Sc is illustrated in Figure 4. It emphasizes that enlarged Sc indicated a reduced diffusion rate, which resulted in a decay in the concentration distribution. Figure 5 presents the influence of the permeability parameter *Re* on the concentration profiles for the fixed values $\varphi_1 = \varphi_2 = 0.01$, $Sc = 1$, $Pr = 6.2$, and $M = 1$. Physically, the Reynolds number demonstrates the ratio of inertial force to viscous force. Figure 5 illustrates that increasing the value of the permeability parameter Re in the center of the wall increased the thickness of the concentration boundary layer.

4. Conclusions

In this article, laminar, MHD, unsteady, and incompressible Newtonian hybrid nanofluid flow combined with the effect of morphology through a deformable porous disk was observed. We used two types of nanoparticles for this purpose: metallic and metallic oxides, with water as the base fluid. By using the software Mathematica with the help of a shooting method based on the fourth-order Runge–Kutta technique, we drew the following results from this research:

- Increasing the numerical values of the magnetic parameter (*M*) and Reynolds number (*Re*) enhanced the values of shear stress in the upper and lower disks;
- Increasing the value of the permeable Reynolds number resulted in opposite flow rates of mass transfer in both porous disks, as shown in the concentration profile;
- The heat transfer rate was enhanced with increased Prandtl number in the presence of hybrid nanoparticles;
- With increasing values of Sc and Re, the flow of mass transfer grew in both porous disks;
- The thermal conductivity of Al_2O_3 + Cu/H_2O hybrid nanofluid flow showed good results with a platelet shape factor at a volume fraction of 4%.

Author Contributions: Investigation, Q.R.; Methodology, M.Z.A.Q.; Software, B.A.K.; Supervision, W.W.; Validation, A.K.H.; Writing—original draft, Q.R. and B.A.; Writing—review & editing, N.A.S. and W.W. All authors have read and agreed to the published version of the manuscript.

Funding: This research received funding support from the NSRF via the Program Management Unit for Human Resources & Institutional Development, Research and Innovation, (grant number B05F650018).

Data Availability Statement: The numerical data used to support the findings of this study are included within the article.

Conflicts of Interest: The authors declare that they have no competing interest.

Nomenclature

B_o	Uniform magnetic field [T]
C_f	Total skin friction coefficient
C_p	Specific heat at constant pressure
k	Dimensionless parameter
M	Magnetic parameter
Pr	Prandtl number
r z	Cylindrical coordinate system
Re	Reynolds number
w	Mass or velocity component along z axis [gr or m/s]
Nu	Nusselt number
ρ_{hnf}	Density for HN_{fd}
ρ_{s2}	Density for second solid NPs
k_{s1}	Thermal conductivity for the first solid fraction
D_{hnf}	Diffusion coefficient of HN_{fd}
k_{mbf}	Thermal conductivity for shape base fluid
k_{bf}	Thermal conductivity for base fluid
μ_{bf}	Viscosity of the base fluid
dp_1	Diameter of first particles
v_{hnf}	Kinematic viscosity for HN_{fd}
F_η	Dimensionless radial velocity profile
θ_η	Dimensionless temperature profile
σ	Electrical conductivity [$(m^3A^2)/kg$]
v	Kinematic viscosity [m^2/s]
μ	Dynamic viscosity [$P_a \cdot s$]
ρ	Density [kg/m^3]
ρC_P	Volumetric heat capacity [$J/(m^3 K)$]
T	HN_{fd} temperature [K]
Sc	Schmidt number

$(\rho c_p)_{hnf}$	Specific heat capacity for HN_{fd}
ρ_{s1}	Density for first solid NPs
k_{hnf}	Thermal conductivity for HN_{fd}
k_{s2}	Thermal conductivity for a second solid fraction
p	Pressure
μ_{eff}	Viscosity for effect
dp	Diameter of particles
dp_2	Diameter of second particles
Sh	Sherwood number
Subscripts	
(b_{fd})	Base fluid
(N_{fd})	Nanofluid
(HN_{fd})	Hybrid nanofluid
(Al_2O_3)	First nanoparticle
(Cu)	Second nanoparticle
Greek symbols	
α	Thermal diffusivity [m^2/s]
η	Independent similarity variable
φ	Equivalent nanoparticle volume fraction
φ_1	Equivalent first nanoparticle volume fraction
φ_2	Equivalent first nanoparticle volume fraction

References

1. Qureshi, M.; Ali, K.; Iqbal, M.F.; Ashraf, M.; Ahmad, S. Heat and mass transfer enhancement of nanofluids flow in the presence of metallic/metallic-oxides spherical nanoparticles. *Eur. Phys. J. Plus* **2017**, *132*, 57W. [CrossRef]
2. Zeeshan, A.; Hassan, M.; Ellahi, R.; Nawaz, M. Shape effect of nanosize particles in unsteady mixed convection flow of nanofluid over disk with entropy generation. *Proc. Inst. Mech. Eng. Part E J. Process Mech. Eng.* **2017**, *231*, 871–879. [CrossRef]
3. Haq, R.U.; Noor, N.F.; Khan, Z.H. Numerical simulation of water based magnetite nanoparticles between two parallel disks. *Adv. Powder Technol.* **2016**, *27*, 1568–1575. [CrossRef]
4. Khan, U.; Ahmed, N.; Mohyud-Din, S.T. Analysis of magnetohydrodynamic flow and heat transfer of Cu–water nanofluid between parallel plates for different shapes of nanoparticles. *Neural Comput. Appl.* **2018**, *29*, 695–703. [CrossRef]
5. Ashraf, M.; Iqbal, I.; Masud, M.; Sultana, N. Numerical prediction of natural convection flow in the presence of weak magnetic Prandtl number and strong magnetic field with algebraic decay in mainstream velocity. *Adv. Appl. Math. Mech.* **2017**, *9*, 349–361. [CrossRef]
6. Qureshi, M.; Rubbab, Q.; Irshad, S.; Ahmad, S.; Aqeel, M. Heat and mass transfer analysis of MHD nanofluid flow with radiative heat effects in the presence of spherical au-metallic nanoparticles. *Nanoscale Res. Lett.* **2016**, *11*, 472. [CrossRef] [PubMed]
7. Devi, S.A.; Devi, R.U. Soret and Dufour effects on MHD slip flow with thermal radiation over a porous rotating infinite disk. *Commun. Nonlinear Sci. Numer. Simul.* **2011**, *16*, 1917–1930. [CrossRef]
8. Xu, H. Modelling unsteady mixed convection of a nanofluid suspended with multiple kinds of nanoparticles between two rotating disks by generalized hybrid model. *Int. Commun. Heat Mass Transf.* **2019**, *108*, 104275. [CrossRef]
9. Mabood, F.; Shateyi, S.; Rashidi, M.M.; Momoniat, E.; Freidoonimehr, N.J. MHD stagnation point flow heat and mass transfer of nanofluids in porous medium with radiation, viscous dissipation and chemical reaction. *Adv. Powder Technol.* **2016**, *27*, 742–749. [CrossRef]
10. Acharya, N.; Bag, R.; Kundu, P.K. Influence of Hall current on radiative nanofluid flow over a spinning disk: A hybrid approach. *Phys. E Low-Dimens. Syst. Nanostruct.* **2019**, *111*, 103–112. [CrossRef]
11. Abbas, A.; Ashraf, M.; Chu, Y.M.; Zia, S.; Khan, I.; Nisar, K.S. Computational study of the coupled mechanism of thermophoretic transportation and mixed convection flow around the surface of a sphere. *Molecules* **2020**, *25*, 2694. [CrossRef] [PubMed]
12. Hussain, M.F.; Akbar, M.Z. Numerical Analysis of Nanofluids with Convective Heat Transfer through Porous Disks. *Casp. J. Comput. Math. Eng.* **2017**, *2*, 5–26.
13. Das, K.; Jana, S.; Acharya, N. Slip effects on squeezing flow of nanofluid between two parallel disks. *Int. J. Appl. Mech. Eng.* **2016**, *21*, 5–20. [CrossRef]
14. Mohyud-Din, S.T.; Khan, S.I.; Bin-Mohsin, B. Velocity and temperature slip effects on squeezing flow of nanofluid between parallel disks in the presence of mixed convection. *Neural Comput. Appl.* **2017**, *28*, 169–182. [CrossRef]
15. Erickson, L.E.; Fan, L.T.; Fox, V.G. Heat and mass transfer in the laminar boundary layer flow of a moving flat surface with constant surface velocity and temperature focusing on the effects of suction/injection. *Ind. Eng. Chem.* **1966**, *5*, 19–25.
16. Zaraki, A.; Ghalambaz, M.; Chamkha, A.J.; Ghalambaz, M.; De Rossi, D. Theoretical analysis of natural convection boundary layer heat and mass transfer of nanofluids: Effects of size, shape and type of nanoparticles, type of base fluid and working temperature. *Adv. Powder Technol.* **2015**, *26*, 935–946. [CrossRef]

17. Turkyilmazoglu, M. Fluid flow and heat transfer over a rotating and vertically moving disk. *Phys. Fluids* **2018**, *30*, 063605. [CrossRef]
18. Mutuku, W.N.; Makinde, O.D. Double stratification effects on heat and mass transfer in unsteady MHD nanofluid flow over a flat surface. *Asia Pac. J. Comput. Eng.* **2017**, *4*, 2. [CrossRef]
19. Reddy, P.S.; Sreedevi, P.; Chamkha, A.J. MHD boundary layer flow, heat and mass transfer analysis over a rotating disk through porous medium saturated by Cu-water and Ag-water nanofluid with chemical reaction. *Powder Technol.* **2017**, *307*, 46–55. [CrossRef]
20. Reddy, P.S.; Rao, K.S. MHD natural convection heat and mass transfer of Al2O3-water and Ag-water nanofluids over a vertical cone with chemical reaction. *Procedia Eng.* **2015**, *127*, 476–484. [CrossRef]
21. Ashraf, M.Z.; Rehman, S.U.; Farid, S.; Hussein, A.K.; Ali, B.; Shah, N.A.; Weera, W. Insight into Significance of Bioconvection on MHD Tangent Hyperbolic Nanofluid Flow of Irregular Thickness across a Slender Elastic Surface. *Mathematics* **2022**, *10*, 2592. [CrossRef]
22. Lou, Q.; Ali, B.; Rehman, S.U.; Habib, D.; Abdal, S.; Shah, N.A.; Chung, J.D. Micropolar Dusty Fluid: Coriolis Force Effects on Dynamics of MHD Rotating Fluid When Lorentz Force Is Significant. *Mathematics* **2022**, *10*, 2630. [CrossRef]
23. Shah, N.A.; Wakif, A.; El-Zahar, E.R.; Ahmad, S.; Yook, S.-J. Numerical simulation of a thermally enhanced EMHD flow of a heterogeneous micropolar mixture comprising (60%)-ethylene glycol (EG), (40%)-water (W), and copper oxide nanomaterials (CuO). *Case Stud. Therm. Eng.* **2022**, *35*, 102046. [CrossRef]
24. Raza, Q.; Qureshi, M.Z.A.; Khan, B.A.; Kadhim Hussein, A.; Ali, B.; Shah, N.A.; Chung, J.D. Insight into Dynamic of Mono and Hybrid Nanofluids Subject to Binary Chemical Reaction, Activation Energy, and Magnetic Field through the Porous Surfaces. *Mathematics* **2022**, *10*, 3013. [CrossRef]
25. Choi, S.U.; Eastman, J.A. *Enhancing Thermal Conductivity of Fluids with Nanoparticles*; Argonne National Lab. (ANL): Argonne, IL, USA, 1995.
26. Nimmagadda, R.; Venkatasubbaiah, K. Conjugate heat transfer analysis of micro-channel using novel hybrid nanofluids (Al_2O_3 + Ag/Water). *Eur. J. Mech.-B/Fluids* **2015**, *52*, 19–27. [CrossRef]
27. Priyadharshini, P.; Archana, M.V.; Ahmmad, N.A.; Raju, C.S.K.; Yook, S.-J.; Shah, N.A. Gradient descent machine learning regression for MHD flow: Metallurgy process. *Int. Commun. Heat Mass Transf.* **2022**, *138*, 106307. [CrossRef]
28. Suresh, S.; Venkitaraj, K.; Selvakumar, P.; Chandrasekar, M. Experimental investigation of mixed convection with synthesis of Al_2O_3-water hybrid nanofluids using two step method and its thermo physical properties. *Colloids Surf.* **2011**, *8*, 41–48. [CrossRef]
29. Sarkar, J.; Ghosh, P.; Adil, A. A review on hybrid nanofluids: Recent research, development and applications. *Renew. Sustain. Energy Rev.* **2015**, *43*, 164–177. [CrossRef]
30. Moghadassi, A.; Ghomi, E.; Parvizian, F. A numerical study of water based Al_2O_3 and Al_2O_3–Cu hybrid nanofluid effect on forced convective heat transfer. *Int. J. Therm. Sci.* **2015**, *92*, 50–57. [CrossRef]
31. Huminic, G.; Huminic, A. Hybrid nanofluids for heat transfer applications–a state-of-the-art review. *Int. J. Heat Mass Transf.* **2018**, *125*, 82–103. [CrossRef]
32. Ashraf, M.; Asghar, S.; Hossain, M. Thermal radiation effects on hydromagnetic mixed convection flow along a magnetized vertical porous plate. *Math. Probl. Eng.* **2010**, *2010*, 686594. [CrossRef]
33. Dushin, V.R.; Smirnov, N.N.; Nikitin, V.F.; Skryleva, E.I.; Weisman, Y.G. Multiple capillary-driven imbibition of a porous medium under microgravity conditions: Experimental investigation and mathematical modeling. *Acta Astronaut.* **2022**, *193*, 572–578. [CrossRef]
34. Dushin, V.R.; Nikitin, V.F.; Smirnov, N.N.; Skryleva, E.I.; Tyurenkova, V.V. Microgravity investigation of capillary driven imbibition. *Microgravity Sci. Technol.* **2018**, *30*, 393–398. [CrossRef]
35. Smirnov, N.N.; Nikitin, V.F.; Skryleva, E.I. Microgravity investigation of seepage flows in porous media. *Microgravity Sci. Technol.* **2019**, *31*, 629–639. [CrossRef]
36. Smirnov, N.N.; Tyurenkova, V.V.; Smirnova, M.N. Laminar diffusion flame propagation over thermally destructing material. *Acta Astronaut.* **2015**, *109*, 217–224. [CrossRef]
37. Wakif, A.; Animasaun, I.L.; Khan, U.; Shah, N.A.; Thumma, T. Dynamics of radiative-reactive Walters-b fluid due to mixed convection conveying gyrotactic microorganisms, tiny particles experience haphazard motion, thermo-migration, and Lorentz force Phys. *Scripta* **2021**, *96*, 125239. [CrossRef]
38. Logvinov, O.A.; Skryleva, E.A. Displacement of a viscous fluid from a Hele-Shaw cell with a sink. *Mosc. Univ. Mech. Bull.* **2016**, *71*, 77–81. [CrossRef]
39. Tyurenkova, V.V.; Smirnova, M.N. Material combustion in oxidant flows: Self-similar solutions. *Acta Astronaut.* **2016**, *120*, 129–137. [CrossRef]
40. Ali, K.; Akbar, M.Z.; Iqbal, M.F.; Ashraf, M. Numerical simulation of heat and mass transfer in unsteady nanofluid between two orthogonally moving porous coaxial disks. *AIP Adv.* **2014**, *4*, 107113. [CrossRef]
41. Sheikholeslami, M.; Ganji, D.D. Nanofluid flow and heat transfer between parallel plates considering Brownian motion using DTM. *Comput. Methods Appl. Mech. Eng.* **2015**, *283*, 651–663. [CrossRef]
42. Qureshi, M.Z.; Ali, K.; Iqbal, M.F.; Ashraf, M. Heat and Mass Transfer Analysis of Unsteady Non-Newtonian Fluid Flow between Porous Surfaces in the Presence of Magnetic Nanoparticles. *J. Porous Media* **2017**, *20*, 1137–1154. [CrossRef]

43. Saba, F.; Ahmed, N.; Khan, U.; Waheed, A.; Rafiq, M.; Mohyud-Din, S.T. Thermophysical analysis of water based (Cu–Al_2O_3) hybrid nanofluid in an asymmetric channel with dilating/squeezing walls considering different shapes of nanoparticles. *Appl. Sci.* **2018**, *8*, 1549. [CrossRef]
44. Majdalani, J.; Zhou, C.; Dawson, C.A. Two-dimensional viscous flow between slowly expanding or contracting walls with weak permeability. *J. Biomech.* **2002**, *35*, 1399–1403. [CrossRef]
45. Ali, K.; Iqbal, M.F.; Akbar, Z.; Ashraf, M. Numerical simulation of unsteady water-based nanofluid flow and heat transfer between two orthogonally moving porous coaxial disks. *J. Theor. Appl. Mech.* **2014**, *52*, 1033–1046. [CrossRef]